Evaluating the physical parameterizations on a coarse grid in the Community Atmosphere Model with spectral-element dynamics

A.R. Herrington[1]*, P.H. Lauritzen[2], S. Goldhaber[2], Mark A. Taylor[3], K.A. Reed[2]

[1]School of Marine and Atmospheric Sciences, Stony Brook University, Stony Brook, New York
[2]National Center for Atmospheric Research, Boulder, Colorado, USA
[3]Sandia National Laboratories, Albuquerque, New Mexico, USA

Key Points:

-
-
-

*Stony Brook, New York

Corresponding author: Adam R. Herrington, `adam.herrington@stonybrook.edu`

Abstract

1 Introduction

Global atmospheric models fundamentally consist of two components. The dynamical core (*dynamics*), which advances the adiabatic equations of motion, and the physical parameterizations (*physics*), which compute the effects of diabatic and subgrid-scale processes (e.g., radiative transfer and moist convection) on the resolved scales. More out of convenience than anything else, the physics are evaluated on the dynamics grid, i.e., the physics grid and dynamics grid coincide. From linear stability and accuracy analysis of numerical methods, it is a common result that the shortest simulated wavelengths are not accurately represented by the dynamical core. Similar arguments can be made though an analysis of the kinetic energy spectra in model simulations [*Skamarock*, 2011]. The grid-scale is therefore under-resolved, leading some to speculate whether the physics should be evaluated on a grid that is more reflective of the scales actually resolved by the dynamical core [*Lander and Hoskins*, 1997; *Williamson*, 2007; *Skamarock*, 2011].

Experimentation with different physics grid resolutions have so far been limited to models employing the spectral transform method [*Lander and Hoskins*, 1997; *Williamson*, 1999; *Wedi*, 2014]. *Lander and Hoskins* [1997] argue that passing under-resolved states to the physics may be even more problematic in spectral transform models, since the physics grid is computed on a transform grid in grid point space, which contains more degrees of freedom than the spectral representation to prevent aliasing of quadratic quantaties. *Wedi* [2014] have experimented with different transform grid resolutions relative to the spectral truncation, and concluded that increasing the resolution in grid-point space relative to the spectral truncation, improves forecast skill. *Wedi* [2014] speculates that the spectral truncation may be thought of as an effective filter, mitigtaing any undesireable artifacts arising from passing under-resolved states to the physics, refuting the concerns of *Lander and Hoskins* [1997]. After the physics forcing is transformed into wave-space, it is straightforward to truncate the physics at any desired wave-number.

Williamson [1999] conducted a convergence study using a global spectral transform model, in which the truncation wave-number of the physics forcing was held fixed, while increasing the resolution of the dynamical core. When the physics and dynamics resolution were increased in tandem, the strength of the Hadley Cell increased montonically with resolution. But when the truncation wave-number of physics forcing was held fixed, the Hadley Cell showed very little sensitivity to dynamical core resolution, resembling the solution for which the dynamics and physics truncation wave-number are the same. The results of *Williamson* [1999] suggest that the dynamical core resolution is aliased to the resolution of the physics forcing.

It is well known that the equations of motion have implicit scale-dependencies at hydrostatic scales [*Orlanski*, 1981]. Perhaps the most dramatic scale depedency occurs under gravitational instability, in which the vertical velocity scales as the inverse of the horizontal scale of the Archimedean buoyancy [*Jeevanjee and Romps*, 2016; *Herrington and Reed*, 2017, 2018]. *Herrington and Reed* [2018] have shown that an increase in horizontal resolution does lead to a reduction in the horizontal scale of the temperature tendencies from the physics, which dictates the Archimedean buoyancy. As a result, larger magnitude vertical motion characterizes the model solution, which *Herrington and Reed* [2017] hypothesizes steers the model towards a new equilibrium.

In contrast to spectral-transform methods, high-order element-based Galerkin methods are prone to grid-imprinting [*Herrington et al.*, in revision], and need be considered when deciding on a physics grid resolution. High-order Galerkin methods are becoming ncreasingly popular in climate and weather applications due to their high-order accuracy (for smooth problems), high-parallel efficiency, high-processor efficiency and geomet-

ric flexibility facilitating mesh-refinement applications, In this study, we develop and implement a coarser physics grid into the Community Atmopshere Model (CAM), with spectral-element dynamics, which uses high-order Galerkin methods, and coupled to the Conservative Semi-Lagrangian Multi-tracer transport scheme [CAM-SE-CSLAM; *Lauritzen et al.*, 2017]. The grid spacing on this physics grid is 1.5 times larger than the tracer transport and dynamics grid. We test the hypothesis, that the coarser physics grid is effective at reducing spurious noise, particularly over regions of rough topography, in CAM-SE-CSLAM.

Any advantages of using a coarser resolution physics grid need be weighed against any potential reduction in the model's effective resolution, which may occur through aliasing of the solution to the coarser physics grid [*Williamson*, 1999]. Section 2 describes the implementation of the coarse physics grid into CAM-SE-CSLAM. Section 3 provides the results of a hierarchy of model configurations to test our hypothesis, and an analysis of the impact of the coarser physics grid on the resolved scales of motion. Section 4 provides a discussion of the results and conclusions.

2 Methods

The mapping algorithm is applied to each element Ω (with spherical area $\Delta\Omega$) so without loss of generality consider one element. Let $\Delta A_k^{(pg)}$ and $\Delta A_\ell^{(cslam)}$ be the spherical area of the physics grid grid cell $A_k^{(pg)}$ and CSLAM control volume $A_\ell^{(cslam)}$, respectively. The physics grid cells and CSLAM cells respectively span the element without gaps or overlaps

$$\cup_{k=1}^{pg^2} A_k^{(pg)} = \Omega \text{ and } A_k^{(pg)} \cap A_\ell^{(pg)} = \emptyset \quad \forall k \neq \ell, \tag{1}$$

$$\cup_{k=1}^{nc^2} A_k^{(cslam)} = \Omega \text{ and } A_k^{(cslam)} \cap A_\ell^{(cslam)} = \emptyset \quad \forall k \neq \ell. \tag{2}$$

The overlap areas between the k-th physics grid cell and CSLAM cells is denoted

$$A_{k\ell} = A_k^{(pg)} \cap A_\ell^{(cslam)}, \tag{3}$$

so that

$$A_k^{(pg)} = \cup_{l=1}^{nc^2} A_{k\ell}. \tag{4}$$

The tendencies from the parameterizations are computed on the physics grid. The tracer tendency in physics grid cell k is denoted $f_k^{(pg)}$. The problem is how to map $f_k^{(pg)}$ to the CSLAM control volumes $f^{(cslam)}$ satisfying the following constraints:

1. **Local mass-conservation**

$$f_k^{(pg)} \Delta p_k^{(pg)} = \cup_{\ell=1}^{nc^2} \Delta A_{k\ell} \Delta p_\ell^{(cslam)} f_\ell^{(cslam)}, \tag{5}$$

where $\Delta p_k^{(pg)}$ is the pressure level thickness in physics grid cell k and similarly for $\Delta p^{(cslam)}$.

2. **Shape-preservation in mixing ratio**: The forcing on the CSLAM grid should not produce a value smaller than the new physics grid mixing ratio, $m_k^{(pg)} + \Delta t f_k^{(pg)}$ or a value smaller than the existing CSLAM mixing ratios over the overlap areas $m_{k\ell}^{(cslam)}$

$$m_k^{(min)} = \min \left(m_k^{(pg)} + \Delta t f_k^{(pg)}, \left\{ m_{k\ell}^{(cslam)} | \ell = 1, nc^2 \right\} \right), \tag{6}$$

where Δt is the physics time-step. Similarly for maxima

$$m_k^{(max)} = \max \left(m_k^{(pg)} + \Delta t f_k^{(pg)}, \left\{ m_{k\ell}^{(cslam)} | \ell = 1, nc^2 \right\} \right), \tag{7}$$

3. **Linear correlation preservation**: The physics forcing must not disrupt linear tracer correlation between species on the CSLAM grid [see, e.g., *Lauritzen and Thuburn*, 2012].

Table 1. Average equatorial grid spacing, Δx, and model time-step, Δx, used by the physical parameterizations, *phys*, and dynamical core, *dyn*.

Grid name	Δx_{dyn}	Δt_{dyn}	Δx_{phys}	Δt_{phys}
ne20pg3	166.8km	300s	166.8km	1800s
ne30pg2	111.2km	300s	166.8km	1800s
ne30pg3	111.2km	300s	111.2km	1800s
ne40pg3	83.4km	150s	83.4km	900s
ne60pg2	55.6km	150s	83.4km	900s
ne60pg3	55.6km	150s	55.6km	900s
ne80pg3	41.7km	75s	41.7km	450s
ne120pg2	27.8km	75s	41.7km	450s
ne120pg3	27.8km	75s	27.8km	450s

4. **Consistency**: A constant mixing ratio tendency, *cnst*, on the physics grid, $f_k^{(pg)} = cnst\ \forall k$, must result in the same (constant) forcing on the CSLAM grid, $f_\ell^{(cslam)} = f_k^{(pg)} = cnst\ \forall \ell$.

To motivate the algorithm that will simultaneously satisfy 1-4 it is informative to discuss how 'standard' mapping algorithms will violate one or more of the constraints.

- Conservative remapping:
- Interpolation:

   some text about how challenging it is to satisfy 1-3 simultaneously

2.1 Algorithm

3 Results

A plethora of grids are developed for CAM-SE-CSLAM (Table 1), and used to understand the sensitivity to physics grid resolution, across a wide range of spectral-element grid resolutions. The physics time-step, Δt_{phys}, used for each grid is scaled by the dynamics time-step to prevent time truncation errors at higher resolutions [*Herrington and Reed*, 2018]. A hierarchy of idealized model configurations are presented (avialble in CESM2.0; https://doi.org/10.5065/D67H1H0V) to illuminate the differences between *pg*2 and *pg*3.

3.1 Moist Baroclinic Wave

   Terminator Test of linear-correlation preservation, and tracer mass conservation (just a number showing to within machine precision).

3.2 Held-Suarez with Topography

Flow over rough topography may facilitate significant grid imprinting using the spectral element method [*Lauritzen et al.*, 2015; *Herrington et al.*, in revision]. A Held-Suarez configuration, modified with real world topography is used to identify grid imprinting over mountainous terrain. Figure 1 (middle panel) shows the climatological mean vertical pressure velocity, ω, over the Andes and Himalayan region and at two different levels in the mid-troposphere, using the *ne30pg3* grid. All Held-Suarez simulations are ran for two-years. The figure is displayed as a raster plot on the native physics grid, so
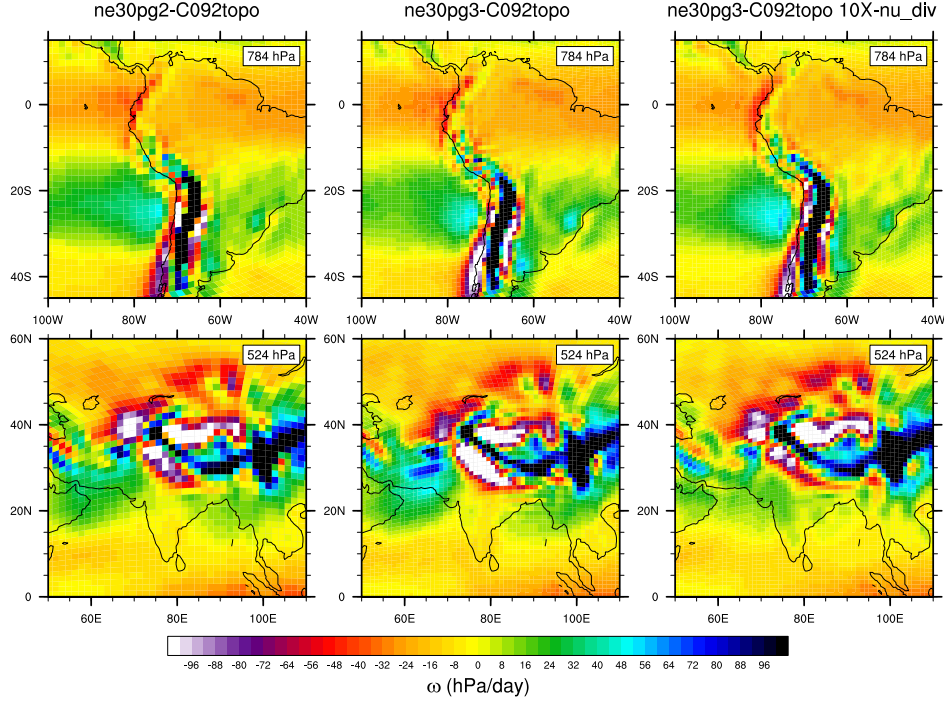
Figure 1. Mean ω at two model levels in the middle troposphere, in a Held-Suarez configuration outfitted with real world topography. (Left) *ne30pg2* (Middle) *ne30pg3* and (Right) *ne30pg3* with the divergence damping coefficient increased by an order of magnitude. The ω fields are computed a two-year simulation. The data are presented on a raster plot in order to identify individual grid cells

that indidual extrema, which characterize the flow over the Andes between about $10° - 20°$ S, may be identified as spurious. Similarly, at the foot of the Himalayas, their appears to be spurious oscillatory bands of upward and downward motion aligned with the element boundaries.

As discussed in *Herrington et al.* [in revision], grid imprinting over the mountains tends to occur in regions of weak stability, and the extrema often manifest as full troposphere upward/downward couplets. Thus, grid imprinting over mountains can be alleviated through increasing the divergence damping in the model. Figure 1 (right panel) repeats the *ne30pg3* simulation, but increasing the divergence damping coefficient by an order of magnitude. The spurious noise over the Andes and the Himalayas are damped, as grid point extrema tends to be diffused into neighboring grid cells. The wave number-power spectrum of the kinetic energy arising from divergent modes is provided in Figure 2, indicating that divergent modes are significantly damped at higher wavenumbers relative to the default *ne30pg3* simulation. Requiring the divergence damping coefficient to be an order of magnitude larger than that required for numerical stability is not ideal from a model development perspective. The hyper-viscosity coefficients are one of the only free-parameters in the dynamical core to tune the kinetic energy spectrum to observations [*Skamarock et al.*, 2014; *Lauritzen et al.*, 2018].

The ω field in a *ne30pg2* simulation is provided in Figure 1 (left panel). Grid cell extrema over the Andes is less prevalent than in the *ne30pg3* simulation, as seen by the reduction in large magnitude ω (red grid cells). The spurious oscillations at the foot of the Himalayas appears to have been entirely eliminated. This improvement in grid imprinting
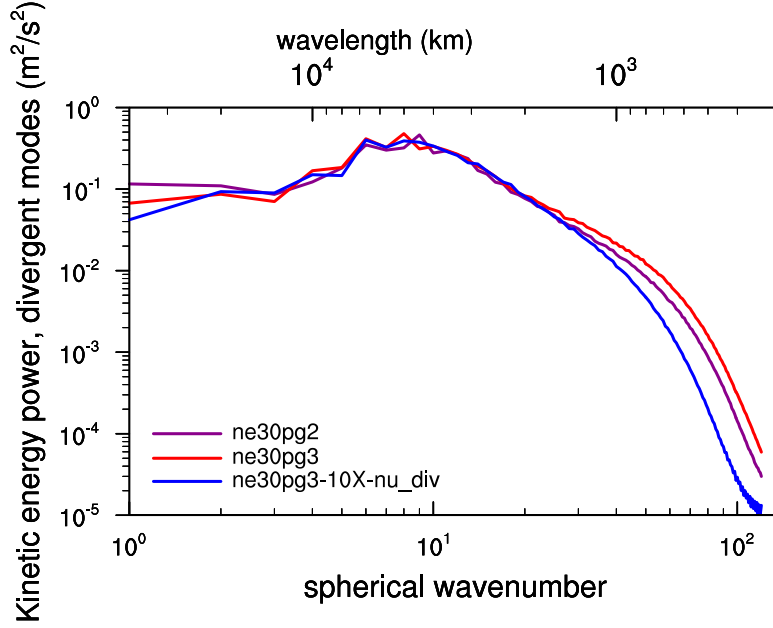
Figure 2. Kinetic energy power spectrum arising from divergent modes in *ne*30*pg*2, *ne*30*pg*3 and *ne*30*pg*3 with the divergence damping coefficient increased by an order of magnitude (*ne*30*pg*3 − 10*X* − *ne_div*).

is due to the homogenization of nodal types in the *pg*2 configuration discussed in Section **??**. The divergent modes are slightly damped relative to the *ne*30*pg*3 simulations, almost sytematically with wavenumber, and much less than the simulation using the larger divergence damping coefficient (Figure 2).

3.3 Aqua-planets

The results of the previous section are consistent with our hypothesis, that spurious noise is effectively reduced, and visibly eliminated using a *pg*2 grid. We now turn to the question of whether the coarser resolution physics grid has an impact on the resolved scales of motion. This analysis will make use of an aqua-planet configuration [*Neale and Hoskins*, 2000; *Medeiros et al.*, 2016]; an ocean covered planet in perpetual equinox, and fixed, zonally-symmetric sea surface temperatures idealized after present day Earth. The aqua-planets are run for one simulated year, using CAM, version 6 physics (CAM6; *QPC*6 compset in CESM2.0).

Herrington and Reed [2017] has shown that through assuming the horizontal scale of the Archimedean buoyancy is linearly proportional to the grid spacing, the magnitude of the vertical motion in a set of aqua-planet runs did not scale like the inverse of the grid-spacing across a set of grid resolutions. However, the results of *Herrington and Reed* [2018] indicate that the scaling may be recovered through a more judicious choice of Δt_{phys} (Table 1). To test this idea, three aqua-planet simulations are carried out using the *ne*30*pg*3, *ne*60*pg*3 and *ne*120*pg*3 grids.

Figure 3a shows the wave-number-power spectrum of the moist physics temperature tendencies (referred to as *forcing* throughout this study) in the upper troposphere, where statiform heating is common due to detrainment by the deep-convection scheme [*Zhang and McFarlane*, 1995]. There is a clear reduction in forcing scale with resolution, which is consistent with the increased magnitude of ω with resolution, expressed by the probability
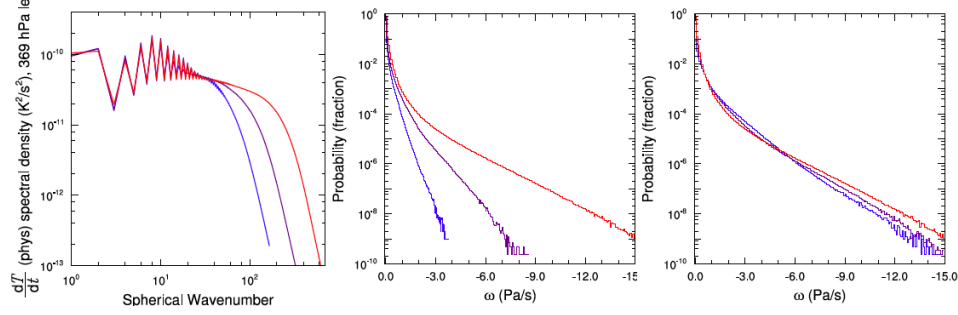
Figure 3. (a) Wavenumber-power spectrum of the temperature tendencies from the moist physics, near the 369 hPa level, (b) probability density distribution and (c) the scaled probability density distribution of upward ω everywhere in the model, from three year long aqua-planet simulations at different grid resolutions.

density distribution (PDF) of upward ω, everywhere in the model (Figure 3b). The PDFs may be scaled to the $ne120pg3$ grid using the scaling of *Pauluis and Garner* [2006],

$$P(\omega_s) = \alpha \times P(\omega/\alpha), \tag{8}$$

where $P(\omega_s)$ is the PDF of the scaled ω, ω_s, and α is the ratio of the vertical velocity scale to the vertical velocity scale of the target grid resolution, set to $\alpha = \Delta x_{target}/\Delta x$, after [*Herrington and Reed*, 2018], where Δx is the grid spacing and Δx_{target} is the grid spacing of the target resolution. The scaled PDFs do not line up perfectly on top one another (Figure 3c), but the scaling explains the change in magnitude of ω with resolution to first order. This result is consistent with the notion that the characteristic forcing scale in the simulations is linearly proportional to the grid spacing.

When the physics and dynamics grids are of a different resolution, it is not clear which grid determines the forcing scale. If the characteristic forcing scale is determined by the physics grid spacing, Δx_{phys}, than the $ne30pg2$ solution should more closely resemble the $ne20pg3$ solution, in which both the physics and dynamics grids are equal to the physics grid of $ne30pg2$. Likewise, if the dynamics grid spacing, Δx_{dyn}, governs the forcing scale than the $ne30pg2$ solution would more closely resemble the $ne30pg3$ solution. Figure 4a is the PDF of upward ω for simluations using the $ne20pg3$, $ne30pg2$ and $ne30pg3$ grids. It is clear that the $ne30pg2$ solution more closely resembles the $ne30pg3$ solution. Scaling the $ne30pg2$ PDF to the $ne30pg3$ grid using Δx_{phys} overestimates the magnitude of ω in the $ne30pg3$ solution, whereas scaling the $ne20pg3$ solution to $ne30pg3$ does a fair job of predicting the $ne30pg3$ magnitudes (Figure 4b).

The dynamical core requires explicit numerical damping to increase with Δx_{dyn} for numerical stability [*Lauritzen et al.*, 2018]. The hyper-viscosity coefficients are therefore smaller (and equal) in the $ne30pg2$ and $ne30pg3$ simulations, relative to the $ne20pg3$ simulation. Figure 4a (green line) shows the PDF of upward ω for a $ne30pg2$ simulation, in which the hyper-viscosity coefficients are increased to $ne20pg3$ values (referred to as $ne30pg2 - hivisc$). The solution now more closely resembles the $ne20pg3$ solution, indicating that an increase in explicit damping results in an increase in characteristic forcing scale. Through scaling the $ne30pg2 - hivisc$ solutions to the $ne30pg3$ grid using Δx_{phys}, the scaled solution lie much closer to the $ne30pg3$ solution, compared wth scaling the default $ne30pg2$ solution using Δx_{phys}. When using a slightly lower resolution physics grid, $\Delta x_{phys}/\Delta x_{dyn} = 1.5$, it seems the forcing scale is primarily determined by Δx_{dyn}, due to Δx_{dyn} dependent hyper-viscous damping.

The vertical velocity scale is determined by the characteristic forcing scale on the dynamical core grid. Mapping the physics forcing to the dynamics grid using a high-order
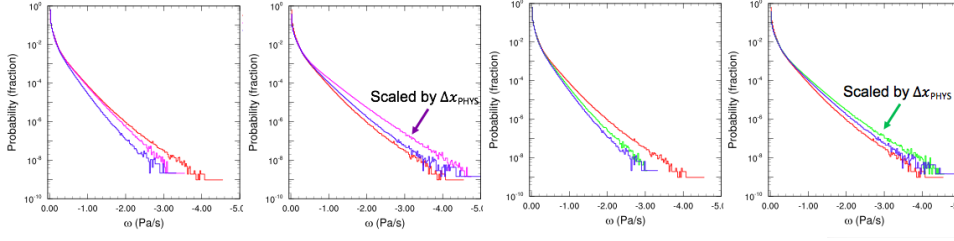
Figure 4. (a) Probability density distribution and (b) the scaled probability density distribution of upward ω everywhere in the model, from four different year long aqua-planet simulations at different grid resolutions. To do: make this a two panel plot with a clear legend.
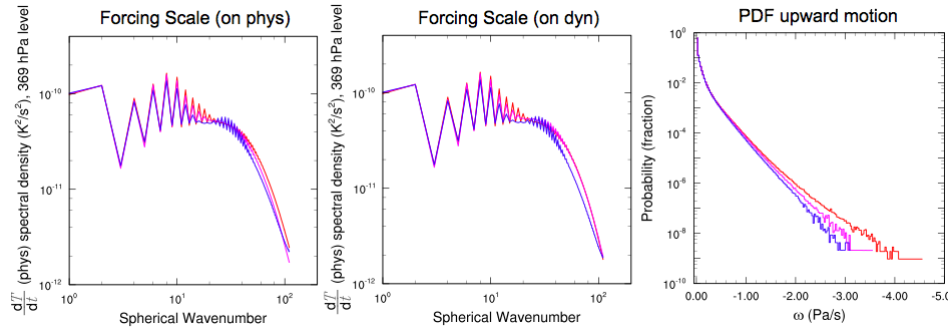

Figure 5. (a) Wavenumber-power spectrum of the temperature tendencies from the moist physics, near the 369 hPa level, on (a) the physics grid, and (b) the dynamics grid, and (c) the probability density distribution of upward ω everywhere in the model To do: make a clear legend.

reconstruction may introduce some fine scale features that the physics grid is unable to support, potentially increasing the vertical velocity scale. A $ne30pg2$ simulation using low-order reconstruction (bilinear interpolation from $pg2$ to GLL, and piecewise-constant mapping between $pg2$ and $CSLAM$ grids; referred to as $ne30pg2 - loworder$) is carried out. The wave-number-power spectrum of the physics forcing in the upper-troposphere on the physics grid (Figure 5a), and after the forcing is mapped to the dynamics grid (Figure 5b) is provided for the $ne30pg2 - loworder$, $ne30pg2$ and $ne30pg3$ simulations.

On the physics grid, power at high wave-numbers is reduced in $ne30pg2 - loworder$ compared with the default $ne30pg2$ solution, and both have less power than the $ne30pg3$ solution at most wave-numbers. On the dynamics grid, $ne30pg2 - lowrder$ is the only solution with a clear reduction in power compared with $ne30pg3$ —the power spectrum of the $ne30pg2$ simulation is indistinguishable from the $ne30pg3$ solution at high wave-numbers (but note the damped oscillations in the $10-20$ wave-number window in $ne30pg2$). The PDFs of upward ω indicate the magnitude of the $ne30pg2$ solution lies intermediate to the two other simulations, but the magnitudes are closer to the $ne30pg3$ solution in the higher probability regions (greater than -2 hPa/day). High-order mapping is therefore an effective means to mitigate any reductions effective resolution arising from the use of a coarser physics grid.

4 Conclusions

References

Herrington, A., and K. Reed (2018), An idealized test of the response of the community atmosphere model to near-grid-scale forcing across hydrostatic resolutions, *J. Adv. Model. Earth Syst.*, *10*(2), 560–575.

Herrington, A., P. Lauritzen, M. A. Taylor, S. Goldhaber, B. E. Eaton, J. Bacmeister, K. Reed, and P. Ullrich (in revision), Physics-dynamics coupling with element-based high-order galerkin methods: quasi equal-area physics grid, *Mon. Wea. Rev.*

Herrington, A. R., and K. A. Reed (2017), An explanation for the sensitivity of the mean state of the community atmosphere model to horizontal resolution on aquaplanets, *J. Climate*, *30*(13), 4781–4797, doi:10.1175/jcli-d-16-0069.1.

Jeevanjee, N., and D. M. Romps (2016), Effective buoyancy at the surface and aloft, *Quart. J. Roy. Meteor. Soc.*, *142*(695), 811–820.

Lander, J., and B. Hoskins (1997), Believable scales and parameterizations in a spectral transform model, *Mon. Wea. Rev.*, *125*, 292–303., doi:10.1175/1520-0493.

Lauritzen, P., and J. Thuburn (2012), Evaluating advection/transport schemes using inter-related tracers, scatter plots and numerical mixing diagnostics, *Quart. J. Roy. Met. Soc.*, *138*(665), 906–918, doi:10.1002/qj.986.

Lauritzen, P. H., J. T. Bacmeister, P. F. Callaghan, and M. A. Taylor (2015), Ncar global model topography generation software for unstructured grids, *Geoscientific Model Development Discussions*, *8*(6), 4623–4651, doi:10.5194/gmdd-8-4623-2015.

Lauritzen, P. H., M. A. Taylor, J. Overfelt, P. A. Ullrich, R. D. Nair, S. Goldhaber, and R. Kelly (2017), CAM-SE-CSLAM: Consistent coupling of a conservative semi-lagrangian finite-volume method with spectral element dynamics, *Mon. Wea. Rev.*, *145*(3), 833–855, doi:10.1175/MWR-D-16-0258.1.

Lauritzen, P. H., R. Nair, A. Herrington, P. Callaghan, S. Goldhaber, J. Dennis, J. T. Bacmeister, B. Eaton, C. Zarzycki, M. A. Taylor, A. Gettelman, R. Neale, B. Dobbins, K. Reed, and T. Dubos (2018), NCAR CESM2.0 release of CAM-SE: A reformulation of the spectral-element dynamical core in dry-mass vertical coordinates with comprehensive treatment of condensates and energy, *J. Adv. Model. Earth Syst.*, doi:10.1029/2017MS001257.

Medeiros, B., D. L. Williamson, and J. G. Olson (2016), Reference aquaplanet climate in the community atmosphere model, version 5, *J. Adv. Model. Earth Syst.*, *8*(1), 406–424, doi:10.1002/2015MS000593.

Neale, R. B., and B. J. Hoskins (2000), A standard test for agcms including their physical parametrizations: I: the proposal, *Atmos. Sci. Lett*, *1*(2), 101–107, doi:10.1006/asle.2000.0022.

Orlanski, I. (1981), The quasi-hydrostatic approximation, *J. Atmos. Sci.*, *38*, 572–582, doi:10.1175/1520-0469(1981)038<0572:TQHA>2.0.CO;2.

Pauluis, O., and S. Garner (2006), Sensitivity of radiative–convective equilibrium simulations to horizontal resolution, *J. Atmos. Sci.*, *63*(7), 1910–1923.

Skamarock, W. (2011), Kinetic energy spectra and model filters, in: P.H. Lauritzen, R.D. Nair, C. Jablonowski, M. Taylor (Eds.), Numerical techniques for global atmospheric models, *Lecture Notes in Computational Science and Engineering, Springer*, *80*.

Skamarock, W. C., S.-H. Park, J. B. Klemp, and C. Snyder (2014), Atmospheric kinetic energy spectra from global high-resolution nonhydrostatic simulations, *Journal of the Atmospheric Sciences*, *71*(11), 4369–4381, doi:10.1175/JAS-D-14-0114.1.

Wedi, N. P. (2014), Increasing horizontal resolution in numerical weather prediction and climate simulations: illusion or panacea?, *Philosophical Transactions of the Royal Society of London A: Mathematical, Physical and Engineering Sciences*, *372*(2018), doi:10.1098/rsta.2013.0289.

Williamson, D. (2007), The evolution of dynamical cores for global atmospheric models, *J. Meteor. Soc. Japan*, *85*, 241–269.

Williamson, D. L. (1999), Convergence of atmospheric simulations with increasing horizontal resolution and fixed forcing scales, *Tellus A*, *51*, 663–673, doi:10.1034/j. 1600-0870.1999.00009.x.

Zhang, G., and N. McFarlane (1995), Sensitivity of climate simulations to the parameterization of cumulus convection in the canadian climate center general-circulation model, *ATMOSPHERE-OCEAN*, *33*(3), 407–446.